

## Comprehensive analysis on the effect of ionic size and size disorder parameter in high entropy stabilized ferromagnetic manganite perovskite

Radhamadhab Das,<sup>1</sup> Sudip Pal<sup>2</sup>,<sup>3</sup> Sudipa Bhattacharya,<sup>1</sup> Shreyashi Chowdhury,<sup>1</sup> Supin K. K.<sup>3</sup>,  
M. Vasundhara<sup>3</sup>, Arup Gayen,<sup>4</sup> and Md. Motin Seikh<sup>1,\*</sup>

<sup>1</sup>Department of Chemistry, Visva-Bharati University, Santiniketan-731235, West Bengal, India

<sup>2</sup>UGC-DAE Consortium for Scientific Research, Indore-452001, India

<sup>3</sup>Polymers and Functional Materials Department, CSIR-Indian Institute of Chemical Technology, Tarnaka, Hyderabad-500007, India

<sup>4</sup>Department of Chemistry, Jadavpur University, Kolkata 700032, India



(Received 4 January 2023; accepted 2 February 2023; published 21 February 2023)

A series of high entropy manganites,  $(5A_{0.2})\text{MnO}_3$ , were prepared with varying the average ionic radius,  $\langle r_A \rangle$ , and cationic size disorder,  $\sigma^2$ , on the A site. All the samples were synthesized using the citrate sol-gel method. In all the compounds, the manganese valence was kept unaltered with reference to the conventional manganite  $\text{La}_{0.6}\text{Sr}_{0.4}\text{MnO}_3$ , which is ferromagnetic with  $T_C \sim 365$  K. The ratio of manganese valance is found to be unaltered as confirmed using x-ray photoelectron studies. The samples were characterized by powder x-ray diffraction, field-emission scanning electron microscopy (FE-SEM), energy dispersive x-ray analysis, elemental mapping, and magnetization measurements. These high entropy oxides show the variation in Curie temperature over a wide range from 85 to 273 K depending on the average A-site ionic radius,  $\langle r_A \rangle$ . A drastic drop down in the ferromagnetic transition temperature of  $T_C = 365$  K for  $\text{La}_{0.6}\text{Sr}_{0.4}\text{MnO}_3$  with  $\langle r_A \rangle = 1.2536$  Å to  $T_C = 137$  K for  $(\text{La}_{0.2}\text{Nd}_{0.2}\text{Gd}_{0.2}\text{Sr}_{0.2}\text{Ba}_{0.2})\text{MnO}_3$  of comparable  $\langle r_A \rangle = 1.2532$  Å can be attributed to the high entropy and/or cationic size disorder effect. The variation of  $T_C$  with  $\langle r_A \rangle$  for the whole series of high entropy manganites does not follow the expected linear behavior; rather, it follows opposite traces of the variation in  $\sigma^2$  with  $\langle r_A \rangle$ . However,  $T_C$  shows almost linear behavior with  $\sigma^2$  except for the sample with lowest  $\langle r_A \rangle$ . This result suggests that the local cationic disordering is more important than the average cationic size in ferromagnetic high entropy manganites. Unlike the conventional system in these high entropy oxides, the ferromagnetic state is not suppressed; only the length scale of the double exchange mediated long-range ferromagnetic interaction is transformed to localized ferromagnetic clusters without losing the ferromagnetic identity. The presence of multiple A-site cations in high entropy oxides results in a local deformation of the  $\text{MnO}_6$  octahedra. This possibly increases the carrier localization followed by reducing the length scale of the double exchange interaction.

DOI: [10.1103/PhysRevMaterials.7.024411](https://doi.org/10.1103/PhysRevMaterials.7.024411)

### I. INTRODUCTION

Since the inception of high entropy alloys in 2004 [1], the design of a multicomponent system to explore the central region of the phase diagram for achieving and tuning a variety of physical properties became an active research field in materials science. The formation of single-phase multicomponent alloys of approximately equimolar mixing has been captured within the framework of increased configurational entropy which originated from the large number of chemical components as well as their respective molar ratio [2]. The configurational entropy change,  $\Delta S_{\text{conf}}$ , is given as  $\Delta S_{\text{conf}} = -R \sum_{i=1}^n x_i \ln x_i$  where  $R$  is the universal gas constant and  $x_i$  is the mole fraction of the  $i$ th element [3].  $\Delta S_{\text{conf}}$  is maximum at equimolar ratio of the components populating a single lattice site. The alteration in chemical compositions to attain the configurational entropy inherently leads to the evolution of different properties of the entropy stabilized phases. This specifically demands a clarification on the actual role of

entropy, the effect of an individual element, the underlying mechanism of phase stability, and the evolved properties. Thus, there is not only the case of entropy stabilization of phases.

Interestingly, these concepts are not only confined to the metallic systems but extended to other kinds of materials such as borides [4], fluorides [5], sulphides [6], carbides [7], aluminosilicides [8], nitrides [9], bixbyite [10], pyrochlore [11–13], magnetoplumbite [14,15], spinels [16,17], oxides, and oxyfluoride [18–20]. However, extension of high entropy concepts on transition metal oxide systems gives a major boost in the research interest on nonmetallic high entropy materials [18]. Transition metal oxides with a plethora of intriguing phenomena are always attractive for applications [21–23]. The tunability of multiple cations on a single site became very appealing in oxide systems. Unlike the high entropy alloys, inclusion of an anion sublattice in oxides provides a broad range of stable structure and accessible functionalities [18,24,25]. In addition, exploration of multicomponent high entropy oxides with extended compositional space of greater flexibility may provide the contemporary requirement of advanced functional materials. In this regard, different kinds

\*Corresponding author: [mdmotin.seikh@visva-bharati.ac.in](mailto:mdmotin.seikh@visva-bharati.ac.in)

of oxides from rocksalts to perovskites and spinels have been investigated [19]. Numerous high entropy materials are reported to exhibit exceptional properties [25–36]. It is amazing that instead of high sensitivity of the magnetic state on bond angle and orbital filling of cations, high entropy oxides with a high level of compositional disordering exhibit long-range magnetic ordering. It is demonstrated that the long-range magnetic ordering prevails not only in simple rocksalt lattice [37–39], but also in complicated spinel and perovskite structures as well [28–30,35]. The entropy stabilized perovskite was reported in 2018 by Jiang *et al.* [31]. There are several reports on high entropy perovskite oxides with multiple cations in the *A* site or the *B* site and even on both sites [17,19,35,40–43]. The magnetic properties of high entropy chromite, ferrite, and cobaltite perovskites with a single transition metal ion in the *B* site and chemical disordering in the *A* site with multiple rare-earth cations exhibit similarities in property to their parent phase [40,44,45]. (Gd<sub>0.2</sub>La<sub>0.2</sub>Nd<sub>0.2</sub>Sm<sub>0.2</sub>Y<sub>0.2</sub>)FeO<sub>3</sub> exhibits highest  $T_N \sim 675$  K and a significant increase in the coercive field [44].

It is well documented that transition metal oxides exhibit subtle energy balance between lattice, spin, charge, and orbital parameters. The important role of local chemical disorder in *ABO*<sub>3</sub> perovskites is well known in the literature [46–52]. In the doped manganite with 30% hole doping the paramagnetic to ferromagnetic transition temperature decreases from 360 to 50 K for decreasing the  $\langle r_A \rangle$  value from 1.24 to 1.18 Å and below  $\langle r_A \rangle = 1.18$  Å, a spin-glass state evolves at the expense of ferromagnetism [53]. The interaction between magnetic cations in perovskites is sensitive to the *M-O* bond length, the *M-O-M* bond angle, lattice distortion, or tilting of *MO*<sub>6</sub> octahedra. The Goldschmidt’s tolerance factor (*f*) scales the orthorhombic distortion and the tilting of the *MO*<sub>6</sub> octahedra [54]. The tolerance factor is defined as  $f = \frac{(r_A+r_O)}{\sqrt{2}(r_B+r_O)}$ , where  $r_A$ ,  $r_B$ , and  $r_O$  are the ionic radii of the *A*-site, *B*-site, and oxygen ions, respectively. Since a major variation is observed for the *A*-site ionic radius compared to that of the *B*-site, the *f* is equivalent to the  $r_A$ ; rather, the average *A*-site cation radius,  $\langle r_A \rangle$ . The effect of *A*-site cations, apart from their magnetic contribution, is strongly reflected from their impact on structural features. The *A*-site cation size determines the *M-O-M* bond angle and hence the magnetic exchange. A clear dependence between  $T_N$  and tolerance *f* is observed in the high entropy oxide perovskite [35,40,44]. The structural distortion is often accompanied by suppression in *A*-site coordination number [55,56], whereas the *B* site is indeed in an ideally octahedral coordination environment irrespective of *A* and *B* sites [40,44]. Another important parameter in perovskite systems is the size disorder parameter. For the  $Ln_{1-x}A_xMO_3$  perovskite, it is defined as  $\sigma^2 = \sum_i x_i r_i^2 - \langle r_A \rangle^2$  where  $\langle r_A \rangle = \sum_i x_i r_i$  is the average ionic radius of the *A*-site cation, and  $x_i$  is the fraction of the *i*th cation of radius  $r_i$  [46,47]. Here  $r_A$  is the standard nine-coordinate ionic radii [57]. The  $r_A$  ranges from 1.216 to 1.083 Å for  $Ln = La-Dy$  and 1.18, 1.31, and 1.47 Å for  $M = Ca, Sr, \text{ and } Ba$ , respectively. A relationship between the chemical disorder and the magnetic exchange has been reported in (Gd, La, Nd, Sm, and/or Y)(Co, Cr, Fe, Mn, and/or Ni)O<sub>3</sub> which exhibits predominant antiferromagnetic ex-

change with small ferromagnetic contribution [35,45], though the exact nature of the magnetic ground state is not clear yet. The design of high entropy oxides based on their ionic radii and oxidation state have been reported in the literature [18,58]. The possible role of  $\sigma^2$  on magnetic behavior is mentioned in high entropy double perovskites [43]. It is worth mentioning that the synergetic effect of multiple cations beyond their size and valence may have an impact on the structure as well as properties. This field is still in its infant stage and the high entropy oxides require further exploration.

A systematic investigation on the effect of ionic radii and size disorder parameter on high entropy perovskite oxides is not thoroughly examined so far. Here, we have addressed this issue by judicious selection of *A*-site cations and by keeping the valence state of *B*-site cations unchanged followed by their physical characterization. We have synthesized a series of high entropy manganite perovskite oxides keeping the central focus on ferromagnetic La<sub>0.6</sub>Sr<sub>0.4</sub>MnO<sub>3</sub>. La<sub>0.6</sub>Sr<sub>0.4</sub>MnO<sub>3</sub> has the highest  $T_C$  of 370 K amongst the La<sub>1-x</sub>Sr<sub>x</sub>MnO<sub>3</sub> series [59]. The *A*-site La<sup>3+</sup> and Sr<sup>2+</sup> are substituted by five different cations keeping the Mn valence ratio fixed (Mn<sup>3+</sup>:Mn<sup>4+</sup>::3:2). The cationic combinations are so selected that the  $r_A$  varies over an appreciable range covering that of the conventional parent La<sub>0.6</sub>Sr<sub>0.4</sub>MnO<sub>3</sub>. A comprehensive account on the effect of  $\langle r_A \rangle$  and  $\sigma^2$  revealed that the latter one is the more dominating one. The increase in  $\sigma^2$  results in fragmentation of the ferromagnetic interaction forming ferromagnetic clusters, without suppression of ferromagnetism.

## II. EXPERIMENTAL DETAILS

### A. Materials synthesis

The polycrystalline powder of the whole series of compounds was prepared by a citrate-based sol-gel method as described in [60]. The starting materials are metal nitrates as received from Sigma-Aldrich. Stoichiometric amounts of desired metal nitrates were weighed and dissolved in 100 ml distilled water. About 2 ml of concentrated nitric acid was added to the solution to avoid hydrolysis of the aquated metal ions. The reaction mixture was continuously stirred for about half an hour using a magnetic stirrer along with a heater. Then, citric acid, about four times the molar ratio of the total metal ions, was added to the solution. The resulting solution was stirred at 80 °C for 3 h. It was then eventually evaporated at 100 °C to form the gel. The gel was dried at 180 °C to obtain the precursor powder. This crude powder was thoroughly ground by an agate mortar pestle, and it was heated at 1200 °C for 24 h inside a platinum crucible container. Finally, the samples were directly quenched to air to stabilize the high entropy phase.

### B. Instrumentation

The powder x-ray diffraction patterns were recorded using a Bruker D8 Advance x-ray diffractometer with Cu  $K\alpha$  radiation ( $\lambda = 1.5418$  Å) operating at 40 kV and 40 mA. The scan speed was regulated with a step size  $\Delta 2\theta = 0.017^\circ$  in the  $2\theta$  range  $10^\circ-100^\circ$ . FE-SEM images, the energy dispersive x-ray (EDX) analyses based cationic composition, and elemental mapping were performed with a Zeiss GeminiSEM 450 field-emission scanning electron microscope at an

accelerating voltage of 20 kV. The nominal cationic compositions were confirmed for all samples from EDX analysis. The PHY 5000 Versa Probe II, ULVAC-PHI, Inc. instrument with an Al  $K\alpha$  x-ray source was employed for the x-ray photoelectron spectroscopy (XPS) characterization in order to know the oxidation states of the samples. The pressure inside the chamber while analyzing was  $5 \times 10^{-10}$  mbar and the C 1s peak located at 284.6 eV was used as the reference peak for the binding energy (B.E.) corrections. The dc-magnetization data were recorded using a 16 T vibrating-sample magnetometer (M/S Quantum Design) working in combination with a variable-temperature cryostat. The magnetic measurements of the samples were performed on compacted powder kept tightly inside a Teflon capsule. The zero-field-cooled (ZFC) and field-cooled (FC) data were recorded in the range 5–380 K. The isothermal magnetization  $M(H)$  was performed at lowest temperatures with an applied field between  $-1$  and  $+5$  T.

### III. RESULTS AND DISCUSSION

#### A. Structural analysis and composition

Figure 1 shows the powder x-ray diffraction patterns of all the high entropy manganites:  $(\text{La}_{0.2}\text{Pr}_{0.2}\text{Nd}_{0.2}\text{Sr}_{0.2}\text{Ba}_{0.2})\text{MnO}_3$ ,  $(\text{La}_{0.2}\text{Nd}_{0.2}\text{Sm}_{0.2}\text{Sr}_{0.2}\text{Ba}_{0.2})\text{MnO}_3$ ,  $(\text{La}_{0.2}\text{Nd}_{0.2}\text{Eu}_{0.2}\text{Sr}_{0.2}\text{Ba}_{0.2})\text{MnO}_3$ ,  $(\text{La}_{0.2}\text{Nd}_{0.2}\text{Gd}_{0.2}\text{Sr}_{0.2}\text{Ba}_{0.2})\text{MnO}_3$ ,  $(\text{La}_{0.2}\text{Pr}_{0.2}\text{Dy}_{0.2}\text{Sr}_{0.2}\text{Ba}_{0.2})\text{MnO}_3$ ,  $(\text{La}_{0.2}\text{Sm}_{0.2}\text{Eu}_{0.2}\text{Sr}_{0.2}\text{Ba}_{0.2})\text{MnO}_3$ ,  $(\text{La}_{0.2}\text{Pr}_{0.2}\text{Nd}_{0.2}\text{Ca}_{0.2}\text{Ba}_{0.2})\text{MnO}_3$  and the conventional  $\text{La}_{0.6}\text{Sr}_{0.4}\text{MnO}_3$ . There is no detectable impurity reflection in the patterns suggesting the formation of single-phase high entropy oxides. The compounds are well crystalline, and the powder patterns can be nicely indexed with the orthorhombic  $Pbnm$  space group. We have carried out Rietveld refinements of all the patterns using the FULPROF SUITE program [61], which are shown in Fig. 1. The details of refinement parameters for all the samples are given in the Supplemental Material (Table S1 [62]). The cell parameters, bond lengths, and bond angles are consistent with manganite perovskite systems. The cell parameters and cell volume systemically increase with the increase in average  $A$ -site ionic radius as expected (Fig. 2). The trend in variation of the bond length and bond angle with  $\langle r_A \rangle$  are included in the Supplemental Material (Fig. S1 [62]). The average  $A$ -O bond distance ( $d_{A-O}$ ) and Mn-O-Mn bond angle show an increasing trend with the increase in  $\langle r_A \rangle$ . However, Mn-O<sub>1</sub> and Mn-O<sub>2</sub> bond distances exhibit a decreasing and increasing trend, respectively, with the increase in  $\langle r_A \rangle$ . The important chemical parameters associated with these high entropy manganite series such as  $\langle r_A \rangle$ ,  $\sigma^2$ , and tolerance factor ( $f$ ) are summarized in Table I. It is worth mentioning that  $\langle r_A \rangle$  and  $f$  run parallelly. This is in agreement with the variation of the standard nine-coordinate ionic radii of the  $A$ -site cations according to their stoichiometry. However,  $\sigma^2$ , which is the variance of the  $A$ -site cations radii distribution, does not follow the linear variation with  $\langle r_A \rangle$  or  $f$ . The particle size and surface morphology of all the powder samples were analyzed by FE-SEM imaging. All the samples show irregular shaped, highly agglomerated, and wide particle size distribution ranging from hundreds of nanometers to microns

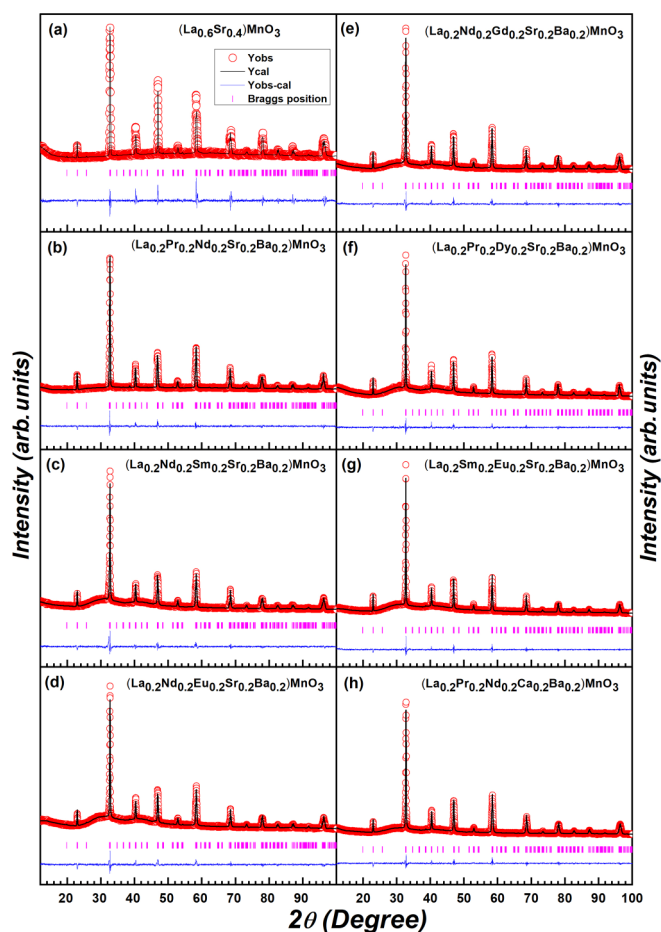


FIG. 1. Powder x-ray diffraction patterns of (a)  $(\text{La}_{0.6}\text{Sr}_{0.4})\text{MnO}_3$ , (b)  $(\text{La}_{0.2}\text{Pr}_{0.2}\text{Nd}_{0.2}\text{Sr}_{0.2}\text{Ba}_{0.2})\text{MnO}_3$ , (c)  $(\text{La}_{0.2}\text{Nd}_{0.2}\text{Sm}_{0.2}\text{Sr}_{0.2}\text{Ba}_{0.2})\text{MnO}_3$ , (d)  $(\text{La}_{0.2}\text{Nd}_{0.2}\text{Eu}_{0.2}\text{Sr}_{0.2}\text{Ba}_{0.2})\text{MnO}_3$ , (e)  $(\text{La}_{0.2}\text{Nd}_{0.2}\text{Gd}_{0.2}\text{Sr}_{0.2}\text{Ba}_{0.2})\text{MnO}_3$ , (f)  $(\text{La}_{0.2}\text{Pr}_{0.2}\text{Dy}_{0.2}\text{Sr}_{0.2}\text{Ba}_{0.2})\text{MnO}_3$ , (g)  $(\text{La}_{0.2}\text{Sm}_{0.2}\text{Eu}_{0.2}\text{Sr}_{0.2}\text{Ba}_{0.2})\text{MnO}_3$ , and (h)  $(\text{La}_{0.2}\text{Pr}_{0.2}\text{Nd}_{0.2}\text{Ca}_{0.2}\text{Ba}_{0.2})\text{MnO}_3$ . The open red circles, black lines, the bottom blue lines, and vertical bars represent the experimental data, calculated pattern, difference curve, and Bragg position, respectively.

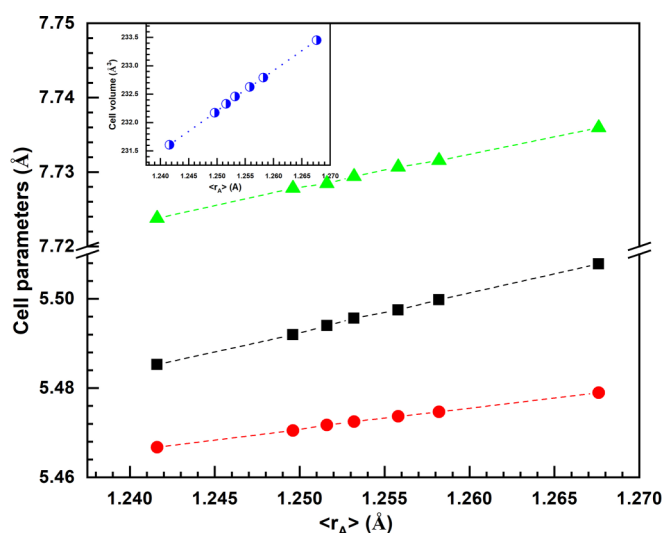


FIG. 2. Variation of cell parameters with  $\langle r_A \rangle$  for the whole series of oxides. Inset shows the variation in cell volume.

TABLE I. Summary of average  $A$ -site ionic radius  $r_A = \sum_i x_i r_i$ ,  $A$ -site size disorder parameter  $\sigma^2 = \sum_i x_i r_i^2 - r_A^2$ , and tolerance factor,  $f = \frac{(r_A + r_O)}{\sqrt{2}(r_B + r_O)}$  of the manganite oxides under investigation.

Composition	$r_A$ (Å)	$f$	$\sigma^2$ (Å <sup>2</sup> )
(La <sub>0.2</sub> Pr <sub>0.2</sub> Nd <sub>0.2</sub> Sr <sub>0.2</sub> Ba <sub>0.2</sub> )MnO <sub>3</sub>	1.2676	0.94362	0.01284
(La <sub>0.2</sub> Nd <sub>0.2</sub> Sm <sub>0.2</sub> Sr <sub>0.2</sub> Ba <sub>0.2</sub> )MnO <sub>3</sub>	1.2582	0.94029	0.01486
(La <sub>0.2</sub> Nd <sub>0.2</sub> Eu <sub>0.2</sub> Sr <sub>0.2</sub> Ba <sub>0.2</sub> )MnO <sub>3</sub>	1.2558	0.93944	0.01549
(La <sub>0.6</sub> Sr <sub>0.4</sub> )MnO <sub>3</sub> (non-HEO)	1.2536	0.93866	0.00212
(La <sub>0.2</sub> Nd <sub>0.2</sub> Gd <sub>0.2</sub> Sr <sub>0.2</sub> Ba <sub>0.2</sub> )MnO <sub>3</sub>	1.2532	0.93852	0.01622
(La <sub>0.2</sub> Pr <sub>0.2</sub> Dy <sub>0.2</sub> Sr <sub>0.2</sub> Ba <sub>0.2</sub> )MnO <sub>3</sub>	1.2516	0.93796	0.01721
(La <sub>0.2</sub> Sm <sub>0.2</sub> Eu <sub>0.2</sub> Sr <sub>0.2</sub> Ba <sub>0.2</sub> )MnO <sub>3</sub>	1.2496	0.93725	0.01680
(La <sub>0.2</sub> Pr <sub>0.2</sub> Nd <sub>0.2</sub> Ca <sub>0.2</sub> Ba <sub>0.2</sub> )MnO <sub>3</sub>	1.2416	0.93442	0.01334

as expected for high-temperature annealed samples. The FE-SEM images, EDX spectra, respective cationic ratio, and elemental mapping for compounds of the whole series are included in the Supplemental Material (Figs. S2–S9 [62]). The EDX spectra were recorded at different areas to confirm the chemical homogeneity and composition. These analyses confirm the nominal stoichiometry with homogeneous cation distribution in all the samples.

The XPS measurements on a selective four samples have been carried out to know about the chemical state and elemental composition present in the material. The obtained binding energies values were calibrated in reference to the C 1s peak, which is located at 284.5 eV. The wide scan XPS spectra of (La<sub>0.2</sub>Nd<sub>0.2</sub>Pr<sub>0.2</sub>Sr<sub>0.2</sub>Ba<sub>0.2</sub>)MnO<sub>3</sub>, (La<sub>0.2</sub>Nd<sub>0.2</sub>Eu<sub>0.2</sub>Sr<sub>0.2</sub>Ba<sub>0.2</sub>)MnO<sub>3</sub>, (La<sub>0.2</sub>Nd<sub>0.2</sub>Gd<sub>0.2</sub>Sr<sub>0.2</sub>Ba<sub>0.2</sub>)MnO<sub>3</sub>, and (La<sub>0.2</sub>Nd<sub>0.2</sub>Pr<sub>0.2</sub>Ca<sub>0.2</sub>Ba<sub>0.2</sub>)MnO<sub>3</sub> shown in the Supplemental Material (Fig. S10 [62]), clearly indicate that there is no impurity present on the surface of the samples other than the expected elements based on the composition. A quantitative analysis of high-resolution slow scan XPS spectra are discussed in the Supplemental Material. The deconvoluted spectra of different samples and the elemental compositions of different chemical states along with the B.E. of elements are available in the Supplemental Material [Figs. S11(a)–S11(c) and Table S2 [62] (see, also, Refs. [63–67] therein)]. The main observation from the XPS analysis is that all the rare-earth and alkaline-earth metals occupied in the  $A$  site exist in +3 and +2 oxidation states, respectively, whereas the  $B$  site exhibits a mixed occupancy of Mn<sup>3+</sup> and Mn<sup>4+</sup> in a desired ratio as expected. So, the occupancy of different rare-earth and alkaline-earth ions in the  $A$  site and the mixed oxidation state of Mn in the  $B$  site are more likely to influence the magnetic properties of all the material.

## B. Magnetic properties

The dc magnetizations for all the samples measured using a 7-T SQUID-vibrating-sample magnetometer under an applied field of 500 Oe between 5 and 380 K are shown in Fig. 3. The scanned temperature range covers the magnetic transition for all the samples. The measurements were done in both the ZFC and the FC protocols. All compositions, except (La<sub>0.2</sub>Pr<sub>0.2</sub>Dy<sub>0.2</sub>Sr<sub>0.2</sub>Ba<sub>0.2</sub>)MnO<sub>3</sub>, exhibit a sharp ferromagnetic type transition. For (La<sub>0.2</sub>Pr<sub>0.2</sub>Dy<sub>0.2</sub>Sr<sub>0.2</sub>Ba<sub>0.2</sub>)MnO<sub>3</sub> the transition is rather sluggish [Fig. 3(f)]. The transition tem-

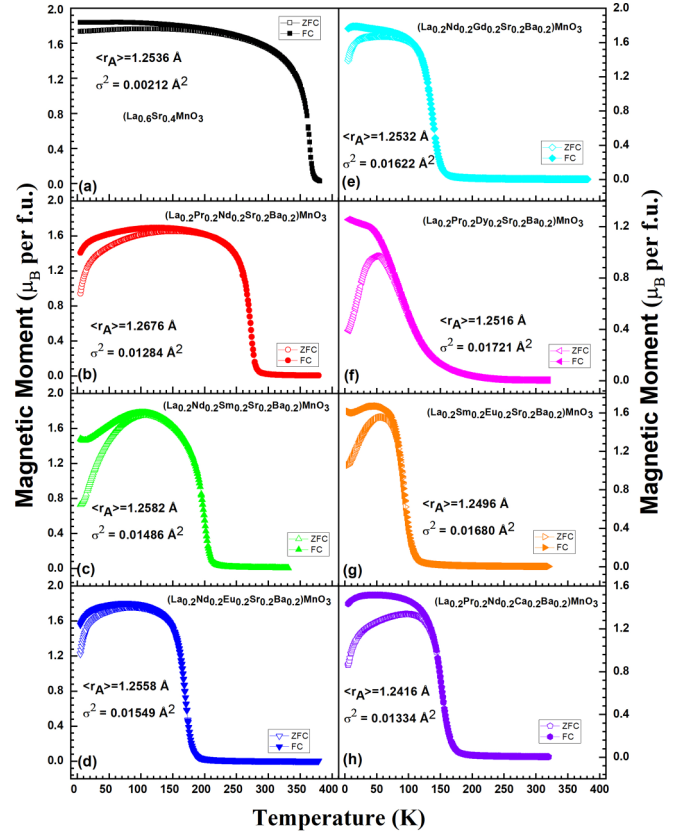


FIG. 3. Temperature-dependent magnetization of (a) (La<sub>0.6</sub>Sr<sub>0.4</sub>)MnO<sub>3</sub>, (b) (La<sub>0.2</sub>Pr<sub>0.2</sub>Nd<sub>0.2</sub>Sr<sub>0.2</sub>Ba<sub>0.2</sub>)MnO<sub>3</sub>, (c) (La<sub>0.2</sub>Nd<sub>0.2</sub>Sm<sub>0.2</sub>Sr<sub>0.2</sub>Ba<sub>0.2</sub>)MnO<sub>3</sub>, (d) (La<sub>0.2</sub>Nd<sub>0.2</sub>Eu<sub>0.2</sub>Sr<sub>0.2</sub>Ba<sub>0.2</sub>)MnO<sub>3</sub>, (e) (La<sub>0.2</sub>Nd<sub>0.2</sub>Gd<sub>0.2</sub>Sr<sub>0.2</sub>Ba<sub>0.2</sub>)MnO<sub>3</sub>, (f) (La<sub>0.2</sub>Pr<sub>0.2</sub>Dy<sub>0.2</sub>Sr<sub>0.2</sub>Ba<sub>0.2</sub>)MnO<sub>3</sub>, (g) (La<sub>0.2</sub>Sm<sub>0.2</sub>Eu<sub>0.2</sub>Sr<sub>0.2</sub>Ba<sub>0.2</sub>)MnO<sub>3</sub>, and (h) (La<sub>0.2</sub>Pr<sub>0.2</sub>Nd<sub>0.2</sub>Ca<sub>0.2</sub>Ba<sub>0.2</sub>)MnO<sub>3</sub> measured under an applied external magnetic field of 500 Oe.

perature,  $T_C$ , is determined from the temperature derivative ( $dM/dT$ ) versus temperature curve in each case (Fig. S12 [62]). The minima in  $dM/dT$  versus temperature plot are taken as  $T_C$ . For the (La<sub>0.2</sub>Pr<sub>0.2</sub>Dy<sub>0.2</sub>Sr<sub>0.2</sub>Ba<sub>0.2</sub>)MnO<sub>3</sub> composition the minima in the temperature-dependent  $dM/dT$  plot are not sharp like other samples. It should be noticed that the transition temperature for the high entropy manganite gradually shifted downwards with the decrease in the average ionic radius of  $A$ -site cations up to  $\langle r_A \rangle = 1.2516$  Å [Figs. 3(b)–3(f)]. On further lowering, the  $\langle r_A \rangle$  value transition temperature shows an upward shift [Figs. 3(g) and 3(h)]. The thermomagnetic irreversibility between the ZFC and FC data is noticed for all samples at lower temperatures. This may be related to the magnetic inhomogeneity at the microscopic scale in perovskite oxides or due to magnetic anisotropy [68–72]. The irreversibility temperature ( $T_{irr}$ ) follows a similar trend as  $T_C$ . The difference between  $T_{irr}$  and  $T_C$  increases with the increase in  $\langle r_A \rangle$ . However, for the (La<sub>0.2</sub>Pr<sub>0.2</sub>Dy<sub>0.2</sub>Sr<sub>0.2</sub>Ba<sub>0.2</sub>)MnO<sub>3</sub> sample  $T_{irr}$  is larger than  $T_C$  and this may be due to the broadening of  $T_C$  for this composition. The  $T_C$  value of the quenched reference (La<sub>0.6</sub>Sr<sub>0.4</sub>)MnO<sub>3</sub> sample is 365 K, which is in excellent agreement to the reported value of 370 K [59,73]. All the high entropy samples,

TABLE II. Summary of the parameters associated with the magnetic properties of the manganite oxides under investigation.

Composition	$T_C$ (K)	$T_{irr}$ (K)	$M_{sat}$ (5 K, 5 T) ( $\mu_B/f.u.$ )	$M_r$ (5 K) ( $\mu_B/f.u.$ )	$H_c$ (5 K) (Oe)	$\mu_{eff}$ ( $\mu_B$ )	$\mu_{cal}$ ( $\mu_B$ ) (including rare-earth contribution)	$\theta_{CW}$ (K)
(La <sub>0.6</sub> Sr <sub>0.4</sub> )MnO <sub>3</sub> (non-HEO)	365	310	3.60	0.259	60.15	5.87	4.52	363.32
(La <sub>0.2</sub> Pr <sub>0.2</sub> Nd <sub>0.2</sub> Sr <sub>0.2</sub> Ba <sub>0.2</sub> )MnO <sub>3</sub>	273	195	3.56	0.901	366.36	6.41	5.07	277.81
(La <sub>0.2</sub> Nd <sub>0.2</sub> Sm <sub>0.2</sub> Sr <sub>0.2</sub> Ba <sub>0.2</sub> )MnO <sub>3</sub>	200	155	3.56	1.23	494.12	7.25	4.86	205.62
(La <sub>0.2</sub> Nd <sub>0.2</sub> Eu <sub>0.2</sub> Sr <sub>0.2</sub> Ba <sub>0.2</sub> )MnO <sub>3</sub>	173	142	3.58	0.782	223.08	7.39	5.05	182.42
(La <sub>0.2</sub> Nd <sub>0.2</sub> Gd <sub>0.2</sub> Sr <sub>0.2</sub> Ba <sub>0.2</sub> )MnO <sub>3</sub>	138	115	4.93	0.934	253.07	7.95	5.98	163.03
(La <sub>0.2</sub> Pr <sub>0.2</sub> Dy <sub>0.2</sub> Sr <sub>0.2</sub> Ba <sub>0.2</sub> )MnO <sub>3</sub>	85	110	4.25	1.262	589.45	7.44	6.75	152.38
(La <sub>0.2</sub> Sm <sub>0.2</sub> Eu <sub>0.2</sub> Sr <sub>0.2</sub> Ba <sub>0.2</sub> )MnO <sub>3</sub>	98	82	3.53	1.08	376.44	7.79	4.83	130.12
(La <sub>0.2</sub> Pr <sub>0.2</sub> Nd <sub>0.2</sub> Ca <sub>0.2</sub> Ba <sub>0.2</sub> )MnO <sub>3</sub>	152	140	3.48	1.02	390.45	7.80	5.07	166.43

except (La<sub>0.2</sub>Pr<sub>0.2</sub>Dy<sub>0.2</sub>Sr<sub>0.2</sub>Ba<sub>0.2</sub>)MnO<sub>3</sub>, exhibit a comparable magnetization value of about  $1.6\mu_B/f.u.$  (Fig. 3). The Gd-containing sample (La<sub>0.2</sub>Nd<sub>0.2</sub>Gd<sub>0.2</sub>Sr<sub>0.2</sub>Ba<sub>0.2</sub>)MnO<sub>3</sub> shows a slightly higher value due to Gd contribution. However, such feature is not reflected for Dy containing (La<sub>0.2</sub>Pr<sub>0.2</sub>Dy<sub>0.2</sub>Sr<sub>0.2</sub>Ba<sub>0.2</sub>)MnO<sub>3</sub>. All the Nd-containing samples show a decrease in magnetization of both the ZFC and FC data at lower temperature [Figs. 3(b)–3(e) and 3(h)]. This may be related to the possible ordering of rare-earth moments.

The isothermal field dependent magnetization was carried out to understand the magnetic ground state of the samples. The  $M(H)$  plots for all the samples were measured under the applied field from  $-1.0$  to  $+5$  T at 5 K, which are available in the Supplemental Material (Fig. S13 [62]). All the samples show practically saturation magnetization at 5 T. However, unlike other samples in (La<sub>0.2</sub>Pr<sub>0.2</sub>Dy<sub>0.2</sub>Sr<sub>0.2</sub>Ba<sub>0.2</sub>)MnO<sub>3</sub> the virgin curve does not coincide with the  $M(H)$  curves [Fig. S13(h) [62]]. This behavior can be related to the weak pinning of the spins particularly in this composition. The saturation magnetization of the quenched (La<sub>0.6</sub>Sr<sub>0.4</sub>)MnO<sub>3</sub> is found to be  $3.60\mu_B/f.u.$ , which is in agreement with the calculated value considering the saturation as  $M_{sat} = g(0.6 \times S_{Mn^{3+}} + 0.4 \times S_{Mn^{4+}}) = (0.6 \times 4\mu_B \text{ of } Mn^{3+} + 0.4 \times 3\mu_B \text{ of } Mn^{4+}) = 3.60\mu_B/f.u.$  (taking the Landé factor as  $g = 2.00$ ). The saturation magnetization of (La<sub>0.2</sub>Nd<sub>0.2</sub>Gd<sub>0.2</sub>Sr<sub>0.2</sub>Ba<sub>0.2</sub>)MnO<sub>3</sub> and (La<sub>0.2</sub>Pr<sub>0.2</sub>Dy<sub>0.2</sub>Sr<sub>0.2</sub>Ba<sub>0.2</sub>)MnO<sub>3</sub> are 4.93 and 4.25  $\mu_B/f.u.$ , respectively, due to contributions from the Gd and Dy ions. The theoretical saturated moments including the rare-earth contribution were calculated by the relationship  $M_{sat} = (0.6 \times 4\mu_B \text{ of } Mn^{3+} + 0.4 \times 3\mu_B \text{ of } Mn^{4+}) + 0.2 \times n_1\mu_B \text{ of } Ln_1^{3+} + 0.2 \times n_2\mu_B \text{ of } Ln_2^{3+}$  (as there are maximum two magnetic rare-earth cations in the investigated samples). Using the  $n$  values 3.58, 3.62, 7.94, and 10.63 for Pr, Nd, Gd, and Dy, respectively, results in  $M_{sat}$  5.92 and 6.44  $\mu_B/f.u.$ , respectively, for (La<sub>0.2</sub>Nd<sub>0.2</sub>Gd<sub>0.2</sub>Sr<sub>0.2</sub>Ba<sub>0.2</sub>)MnO<sub>3</sub> and (La<sub>0.2</sub>Pr<sub>0.2</sub>Dy<sub>0.2</sub>Sr<sub>0.2</sub>Ba<sub>0.2</sub>)MnO<sub>3</sub>. The higher calculated values compared to the observed isothermal magnetization curves may be due to partial alignment of the rare earth under the applied field. For other samples the values are marginally lower than the calculated value (Table II). The shape of the  $M(H)$  curves confirms the soft ferromagnetic nature of the samples. The rapid increase in magnetization in  $M(H)$  curves can be attributed to the domain motion of the soft

ferromagnet as reported for the La<sub>1-x</sub>Sr<sub>x</sub>MnO<sub>3</sub> series [59]. The coercive field and remanent magnetization vary from 0.78 to 1.26  $\mu_B/f.u.$  and 200 to 500 Oe, respectively, for all the high entropy samples. However, these values are significantly larger than that of the conventional (La<sub>0.6</sub>Sr<sub>0.4</sub>)MnO<sub>3</sub> phase (see Table II).

Valuable information about the magnetic character of the samples can be obtained from fitting of the inverse magnetic susceptibility  $\chi^{-1}(T)$  data using Curie-Weiss law  $\chi^{-1} = \frac{(T-\theta_{CW})}{C}$ . Figure 4 shows the temperature-dependent inverse magnetic susceptibility of the FC data for all the samples. A linear fit to the whole high-temperature regime of  $\chi^{-1}(T)$  is achieved above  $T_C$  for samples with  $\langle r_A \rangle$  value up to 1.2582 Å [Figs. 4(a)–4(c)]. The appearance of deviation from linearity in  $\chi^{-1}(T)$  is noticed for  $\langle r_A \rangle \leq 1.2558$  Å [Figs. 4(d)–4(h)]. Except for (La<sub>0.2</sub>Pr<sub>0.2</sub>Dy<sub>0.2</sub>Sr<sub>0.2</sub>Ba<sub>0.2</sub>)MnO<sub>3</sub>, all other samples show upward deviation. The  $\chi^{-1}(T)$  plot of (La<sub>0.2</sub>Pr<sub>0.2</sub>Dy<sub>0.2</sub>Sr<sub>0.2</sub>Ba<sub>0.2</sub>)MnO<sub>3</sub> rather resembles a Griffith-like phase as observed in La<sub>0.4</sub>Ca<sub>0.3</sub>Sr<sub>0.3</sub>MnO<sub>3</sub> [74]. The Curie-Weiss temperatures,  $\theta_{CW}$ , are positive for the series confirming the ferromagnetic nature of the samples. The  $\theta_{CW}$  and extracted effective moment,  $\mu_{eff}$ , for all samples, along with other magnetic parameters, are summarized in Table II. The  $\mu_{eff}$  values for all compositions are higher than the calculated values.

#### IV. DISCUSSION

Here we attempted to understand the observed magnetic behavior of the whole series. The three factors which mostly account for the physical properties of the doped perovskite manganite  $Ln_{1-x}M_xMnO_3$  ( $Ln$  = rare-earth ion,  $M$  = divalent ion) are (i) the hole doping level  $x$ , (ii)  $\langle r_A \rangle$ , the average  $A$ -site ionic radius, and (iii)  $\sigma^2$ , the  $A$ -site cation disordering, which is measured by the variance of the  $A$ -site cation radius distribution [46–47, 75–78]. The increase in  $\langle r_A \rangle$  broadens the electronic bandwidth and facilitates the electronic conduction by widening the Mn-O-Mn bond angle [79, 80]. Thus, the system with a larger  $\langle r_A \rangle$  value will exhibit higher  $T_C$  for a fixed level of hole doping. The strong dependence of  $T_C$  on  $\langle r_A \rangle$  in the manganite system has been reported by several authors suggesting a very strong electron-lattice coupling [53, 81–84]. This coupling is evidenced by oxygen isotope effect [85], striction couple magnetoresistance [86], or magnetic

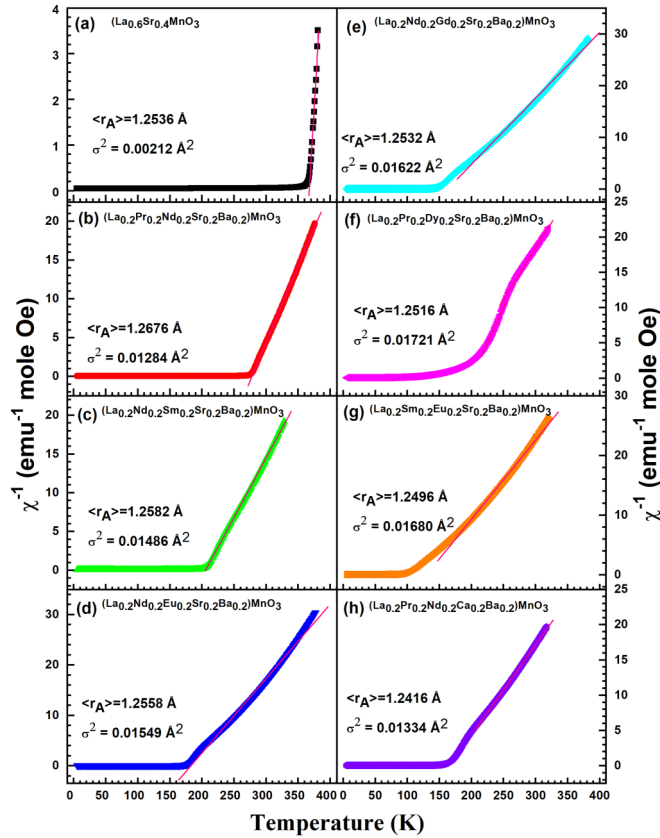


FIG. 4. Temperature-dependent  $\chi^{-1}$  plot of (a)  $(\text{La}_{0.6}\text{Sr}_{0.4})\text{MnO}_3$ , (b)  $(\text{La}_{0.2}\text{Pr}_{0.2}\text{Nd}_{0.2}\text{Sr}_{0.2}\text{Ba}_{0.2})\text{MnO}_3$ , (c)  $(\text{La}_{0.2}\text{Nd}_{0.2}\text{Sm}_{0.2}\text{Sr}_{0.2}\text{Ba}_{0.2})\text{MnO}_3$ , (d)  $(\text{La}_{0.2}\text{Nd}_{0.2}\text{Eu}_{0.2}\text{Sr}_{0.2}\text{Ba}_{0.2})\text{MnO}_3$ , (e)  $(\text{La}_{0.2}\text{Nd}_{0.2}\text{Gd}_{0.2}\text{Sr}_{0.2}\text{Ba}_{0.2})\text{MnO}_3$ , (f)  $(\text{La}_{0.2}\text{Pr}_{0.2}\text{Dy}_{0.2}\text{Sr}_{0.2}\text{Ba}_{0.2})\text{MnO}_3$ , (g)  $(\text{La}_{0.2}\text{Sm}_{0.2}\text{Eu}_{0.2}\text{Sr}_{0.2}\text{Ba}_{0.2})\text{MnO}_3$ , and (h)  $(\text{La}_{0.2}\text{Pr}_{0.2}\text{Nd}_{0.2}\text{Ca}_{0.2}\text{Ba}_{0.2})\text{MnO}_3$ . The solid lines are Curie-Weiss fit to the experimental data at higher temperature.

field sensitivity of lattice distortion [87]. However, this linear relationship between  $T_C$  and  $\langle r_A \rangle$  does not hold for the present high entropy series with 40% hole doping. Figure 5 shows the variation of  $T_C$  of this series of high entropy manganite. There is a decrease in  $T_C$  with the increase in  $\langle r_A \rangle$  from 1.2416 Å, though there is a monotonous increase in lattice parameters and cell volume with the increase in  $\langle r_A \rangle$  (Fig. 2). Above  $\langle r_A \rangle = 1.2516$  Å  $T_C$  increases with  $\langle r_A \rangle$  as expected. This suggests that  $T_C$  is not a single function of  $\langle r_A \rangle$ . On the other hand, an increase in  $\sigma^2$  destabilizes the Mn-O-Mn bond angle and the bond length. This eventually spreads and interrupts the magnetic Mn-O-Mn network in the lattice. This intrinsic factor plays a crucial role to create disorder and inhomogeneity in the system as well. Thus  $\langle r_A \rangle$  and  $\sigma^2$  have an antagonist effect. The effect of  $\sigma^2$  on properties can be examined in three different ways such as (i) variation of  $\sigma^2$  for a fixed  $\langle r_A \rangle$  value which is mostly carried out, (ii) both  $\langle r_A \rangle$  and  $\sigma^2$  can be varied, and (iii) both  $\langle r_A \rangle$  and  $\sigma^2$  are varied to maintain the constant  $T_C$  [78]. Unlike the conventional oxides, due to the restriction in selecting a composition keeping the Mn valence unaltered, we have varied both the  $\langle r_A \rangle$  and the  $\sigma^2$  by avoiding provision (i). Figure 5(a) shows that the variation of  $T_C$  and  $\sigma^2$  with  $\langle r_A \rangle$  follow each other in a reciprocal way. At

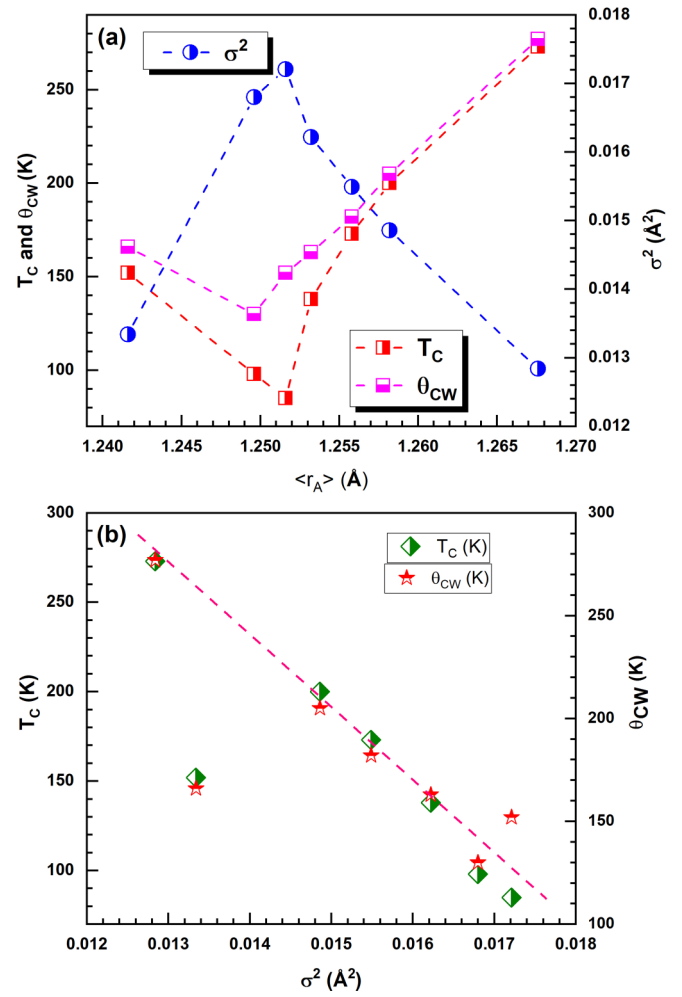


FIG. 5. (a) Variation of  $T_C$ ,  $\theta_{CW}$ , and the size variance ( $\sigma^2$ ) with the A-site ionic radius,  $\langle r_A \rangle$  for the high entropy oxides, and (b) variation of  $T_C$  and  $\theta_{CW}$  as a function of the size variance,  $\sigma^2$ .

this point it is worth noting that where  $T_C$  decreases with an increase in  $\langle r_A \rangle$  as mentioned above, the  $\sigma^2$  value increases and reaches a maximum of  $0.01721 \text{ \AA}^2$  at  $1.2516 \text{ \AA}$ . Afterward  $\sigma^2$  decreases with the increase in  $\langle r_A \rangle$  and  $T_C$  exhibits normal dependence on it. This suggests that the effect of  $\sigma^2$  is rather dominating for this series of high entropy oxide. Accordingly, it is expected that  $T_C$  should vary linearly with  $\sigma^2$ . In fact, it is observed that except for  $(\text{La}_{0.2}\text{Pr}_{0.2}\text{Nd}_{0.2}\text{Ca}_{0.2}\text{Ba}_{0.2})\text{MnO}_3$   $T_C$  for other compositions follow a linear relationship with  $\sigma^2$  as shown in Fig. 5(b). Interestingly, though the  $\sigma^2$  value of  $(\text{La}_{0.2}\text{Pr}_{0.2}\text{Nd}_{0.2}\text{Ca}_{0.2}\text{Ba}_{0.2})\text{MnO}_3$  is  $0.01334 \text{ \AA}^2$ , it has the lowest  $\langle r_A \rangle = 1.2416 \text{ \AA}$  value. The highest  $T_C$  (273 K) observed for  $(\text{La}_{0.2}\text{Pr}_{0.2}\text{Nd}_{0.2}\text{Sr}_{0.2}\text{Ba}_{0.2})\text{MnO}_3$  in the series has the highest  $\langle r_A \rangle = 1.2676 \text{ \AA}$  and lowest  $\sigma^2 = 0.01284 \text{ \AA}^2$ . If we compare the  $\langle r_A \rangle$  of  $(\text{La}_{0.2}\text{Pr}_{0.2}\text{Nd}_{0.2}\text{Sr}_{0.2}\text{Ba}_{0.2})\text{MnO}_3$  ( $1.2676 \text{ \AA}$ ) and  $(\text{La}_{0.2}\text{Pr}_{0.2}\text{Nd}_{0.2}\text{Ca}_{0.2}\text{Ba}_{0.2})\text{MnO}_3$  ( $1.2416 \text{ \AA}$ ), they are compositionally different only by Sr and Ca. It appears that due to the replacement of Sr by Ca  $\langle r_A \rangle$  drops by  $0.0263 \text{ \AA}$  and  $\sigma^2$  by  $0.0005 \text{ \AA}^2$ . Thus, though  $\sigma^2$  is comparable, the large drop in  $T_C$  from 273 K for the Sr composition to 152 K in the Ca composition is about

120 K pushing it as an outlier. This suggests the dominating role of  $\langle r_A \rangle$  in addition to  $\sigma^2$  in HEO manganite.  $\theta_{CW}$  versus  $\sigma^2$  is coplotted with  $T_C$  in Fig. 5(b) and it shows similar behavior as  $T_C$ . However, the  $\theta_{CW}$  for highest  $\sigma^2$  composition show a slight deviation which may be due to the sluggish transition in  $(\text{La}_{0.2}\text{Pr}_{0.2}\text{Dy}_{0.2}\text{Sr}_{0.2}\text{Ba}_{0.2})\text{MnO}_3$  as discussed above.

We will now focus on the magnetic behavior observed for  $(\text{La}_{0.2}\text{Pr}_{0.2}\text{Dy}_{0.2}\text{Sr}_{0.2}\text{Ba}_{0.2})\text{MnO}_3$ . This composition has an intermediate value of  $\langle r_A \rangle = 1.2516 \text{ \AA}$  and highest  $\sigma^2 = 0.017 \text{ 21 \AA}^2$ . It shows a continuous magnetic transition [Figs. 3(f) and Fig. S12(f)] with lowest  $T_C$  and distinct features in the  $M(H)$  curve [Fig. S12(f) [62]]. At a very large value of  $\sigma^2$  due to large size disparities between the A-site cations results in inhomogeneities at microscopic level, though it appears as a single phase in x-ray diffraction. This eventually leads to the fragmentation of the ferromagnetic state. The appearance of a double electrical transition in  $\text{Nd}_{0.15}\text{Sm}_{0.55}\text{Ba}_{0.25}\text{Sr}_{0.05}\text{MnO}_3$  with  $\sigma^2 = 0.0207 \text{ \AA}^2$  has been attributed to the phase inhomogeneity [75,88]. This situation appears above  $\sigma^2 = 0.015 \text{ \AA}^2$  for  $\text{Ln}_{0.7}\text{M}_{0.3}\text{MnO}_3$  manganite and  $T_C$  does not remain a simple function of  $\sigma^2$  [69]. In the present series with 40% hole doping, we did not observe significant deviation from linearity in  $T_C$  for  $\sigma^2$  values 0.0168 and  $0.017 \text{ 21 \AA}^2$  [Fig. 5(b)] as in the case of  $\text{Ln}_{0.7}\text{M}_{0.3}\text{MnO}_3$  [75]. Several reports from different groups on critical behavior analysis of magnetization around the Curie temperature in a large band width manganite system suggest the prevalence of magnetic inhomogeneity which is associated with the cationic size mismatch [50,68,89], quenched disorder [90], or disorder-induced correlation between charge, spin, and lattice degrees of freedom [75,91,92].

Here, it is worth mentioning that the minima in the  $dM/dT$  versus  $T$  plot for  $(\text{La}_{0.2}\text{Pr}_{0.2}\text{Dy}_{0.2}\text{Sr}_{0.2}\text{Ba}_{0.2})\text{MnO}_3$  is extended over a 20 K width of temperature (Fig. S12 [62]). This suggests that the transition is not a long-range ferromagnetic type. A possible short-range magnetic interaction is present in the system which may lead to clustering as reflected from the effective magnetic moments observed in the paramagnetic region. The ferromagnetic metallic system can be converted into insulating cluster glass with enhanced cationic disordering in the A site [47,89,90]. Even the strength of double exchange interactions responsible for ferromagnetism in manganites is distributed with the increase in disordering which results in the broadening in  $T_C$  [91]. The presence of quenched disorder or the existing disorder in the system assist the appearance and stabilization of the short-range magnetic interaction or the Griffith phase at the above  $T_C$  [74,93,94]. The inverse susceptibility plot of  $(\text{La}_{0.2}\text{Pr}_{0.2}\text{Dy}_{0.2}\text{Sr}_{0.2}\text{Ba}_{0.2})\text{MnO}_3$  exhibits a Griffith-like feature as observed in  $\text{La}_{0.4}\text{Ca}_{0.3}\text{Sr}_{0.3}\text{MnO}_3$  [74]. The observed colossal magnetoresistance in manganite systems has been explained within the context of Griffiths [91,92,95]. Several experimental data support the primordial role of quench disorder in the development of the Griffith phase [91,96,97].

However, the  $M(H)$  behavior of the samples available in the Supplemental Material (Fig. S13 [62]), reveals some interesting features on these high entropy oxides. Though the ferromagnetic ordering temperature varies over a wide range from 85 to 273 K, all the samples show a rapid increase in

magnetization in  $M(H)$  curves (Fig. S13 [62]) and they show the saturation magnetization close to the theoretical values (Table II). This suggests that ferromagnetic contribution is not suppressed or there is an evolution of other magnetic states such as antiferromagnetic or glassy phase. This contrasts with the conventional oxides investigated with  $\sigma^2$  variation, where large A-site disorder is unfavorable to the stabilization of the ferromagnetism and develop antiferromagnetic or glassy phase [89,98–103]. All the samples are soft ferromagnets and magnetization saturation attends through the domain motion [59]. Only the  $(\text{La}_{0.2}\text{Pr}_{0.2}\text{Dy}_{0.2}\text{Sr}_{0.2}\text{Ba}_{0.2})\text{MnO}_3$  composition shows a slight anomaly in the  $M(H)$  virgin curve, which is most likely associated to the weak pinning of the spins [Fig. S13(h) [62]]. Thus, unlike in conventional manganite where the ferromagnetic state is suppressed with an increase in  $\sigma^2$  or a decrease in  $\langle r_A \rangle$ , in high entropy manganite the smaller  $\langle r_A \rangle$  values result in a decrease in the Mn-O-Mn bond angles, which weakens the ferromagnetic double exchange interaction. On the other hand, the enhanced size disorder  $\sigma^2$  causes a local deformation of the  $\text{MnO}_6$  octahedra, which can increase carrier localization. Such localization was suggested to be related to the Anderson localization of the fully spin polarized  $e_g$  carriers in the  $\text{La}_{1-x}\text{Sr}_x\text{MnO}_3$  series [59]. This observation suggests that the B-site magnetic exchange interaction is fragmented by multiple cation substitution in high entropy manganites and even has nothing to do with the existence of A-site magnetism. The long-range ferromagnetic ordering is transformed to the short-range ordered ferromagnetic clusters without losing the ferromagnetic identity or evolution of any other magnetic states such as antiferromagnetic or glassy states.

In Fig. 5(a) we have shown that the  $T_C$  and  $\theta_{CW}$  are almost the same for higher  $\langle r_A \rangle$  values. However, the deviation between  $T_C$  and  $\theta_{CW}$  progressively increases with the decrease in  $\langle r_A \rangle$  and increase in  $\sigma^2$ . This difference again reduced for lower values of  $\sigma^2$  even with lowering in  $\langle r_A \rangle$  value [Fig. 5(a)]. Generally,  $T_C$  and  $\theta_{CW}$  remain almost the same if long-range ferromagnetic ordering prevails in the system. The observed deviation between  $T_C$  and  $\theta_{CW}$  has been attributed to the formation of ferromagnetic clusters in the system with an increase in cation disordering [50]. Furthermore, the experimental  $\mu_{\text{eff}}$  values of all the samples are larger than the theoretically calculated effective magnetic moment  $\mu_{\text{eff}} = \sqrt{0.6 \times \mu_{\text{Mn}^{3+}}^2 + 0.4 \times \mu_{\text{Mn}^{4+}}^2} = 4.52 \mu_B/\text{f.u.}$  (see Table II). Even after including the rare-earth contribution following the relation  $\mu_{\text{eff}} = \sqrt{0.2 \times \mu_{\text{Ln}^{3+}}^2 + 0.2 \times \mu_{\text{Ln}^{3+}}^2 + 0.6 \times \mu_{\text{Mn}^{3+}}^2 + 0.4 \times \mu_{\text{Mn}^{4+}}^2}$  (as there are maximum two rare earths each of 0.2 weightage that can contribute to the moment), the calculated effective moments are still below the observed value. The values including rare-earth contribution are shown in Table II. The inverse susceptibility data for  $\langle r_A \rangle = 1.2558 \text{ \AA}$  onward show the upward deviation [Figs. 4(d)–4(h)]. The upward deviation in susceptibility, larger  $\mu_{\text{eff}}$  values than the calculated one, and different values of  $T_C$  and  $\theta_{CW}$  support the formation of ferromagnetic clusters [49,50,52]. Thus, it can be concluded that in these high entropy manganites the double exchange mediated long-range ferromagnetic interaction is broken with the increase in cationic disordering, eventually resulting

in the formation of ferromagnetic clusters. The magnetic nature of the high-temperature region particularly when the system is approaching toward magnetic phase transition will be worth investigating. The high entropy effect provides the opportunity to tune the physical properties in the manganite system, but at the same time it needs to compromise the  $T_C$  which is shifted downward due to induced disordering in the system. Another important issue is to clarify whether it is the high entropy effect or the intrinsic cation size disorder that plays the actual role, particularly in the manganite system.

## V. CONCLUSIONS

A series of high entropy ferromagnetic manganites with fixed hole doping has been investigated to understand the role of high entropy effect. In this connection, the relevance of the two well-known parameters, namely, average  $A$ -site ionic radius,  $\langle r_A \rangle$ , and  $\sigma^2$ , the  $A$ -site cation disordering, which mostly describe the physical properties of manganites, are seriously considered to understand our results. All the samples were thoroughly characterized using powder x-ray diffraction, FE-SEM, EDX analysis, elemental mapping, and magnetization measurements. XPS studies confirmed that the ratio of  $\text{Mn}^{3+}$  to  $\text{Mn}^{4+}$  valance is found to be unaltered for the high entropy effect. The common observation of an increase in  $T_C$  with  $\langle r_A \rangle$  in manganite does not stand in this high entropy series. A decrease in  $T_C$  with the increase in  $\langle r_A \rangle$  from 1.2416 to 1.2516 Å is observed, though there is a monotonous increase in cell parameters and cell volume with the increase in  $\langle r_A \rangle$ , which suggests that  $T_C$  is not a single function of  $\langle r_A \rangle$ . The effect of  $\sigma^2$  is rather dominating for this series of high entropy oxides.

Though  $T_C$  in the series varies over a wide temperature range from 85 to 273 K, all the samples show strong ferromagnetic behavior without evolution of other magnetic states such as antiferromagnetic or frustrated states. This is in contrast to the conventional manganite where large  $\sigma^2$  destabilize the ferromagnetism and develop antiferromagnetic or glassy phase. The  $B$ -site magnetic exchange interaction is fragmented by multiple cation substitutions in high entropy manganites. The local lattice distortion around the multiple cations results in deformation of the  $\text{MnO}_6$  octahedra, which possibly increases carrier localization reducing the length scale of the double exchange interaction. This transforms the long-range ferromagnetic ordering to ferromagnetic clusters without losing the ferromagnetic identity or evolution of any other magnetic states such as antiferromagnetic or glassy states. The existence of  $A$ -site magnetism does not influence the  $B$ -site interaction.

## ACKNOWLEDGMENTS

The authors gratefully acknowledge financial support from the Science and Engineering Research Board (SERB), Government of India, by Grant No. CRG/2021/000342 to Md. M. Seikh. The authors gratefully acknowledge Dr. Rajeev Rawat, UGC-DAE Consortium for Scientific Research, Indore, India for the magnetic measurements and Mr. Suman Karmakar for assisting with magnetic data collection. M. Vasundhara would like to acknowledge the support offered by Department of K&IM of Indian Institute of Chemical Technology (IICT/Pubs./2023/046).

The authors declare that there is no conflict of interest regarding the publication of this paper.

- 
- [1] B. Cantor, I. T. H. Chang, P. Knight, and A. J. B. Vincent, *Mater. Sci. Eng. A* **375**, 213 (2004).
- [2] J. W. Yeh, S. K. Chen, S. J. Lin, J. Y. Gan, T. S. Chin, T. T. Shun, C. H. Tsau, and S. Y. Chang, *Adv. Eng. Mater.* **6**, 299 (2004).
- [3] B. S. Murty, J. W. Yeh, and S. Ranganathan, *High-Entropy Alloys* (Butterworth-Heinemann, London, 2014).
- [4] J. Gild, Y. Zhang, T. Harrington, S. Jiang, T. Hu, M. C. Quinn, W. M. Mellor, N. Zhou, K. Vecchio, and J. Luo, *Sci. Rep.* **6**, 37946 (2016).
- [5] X. Chen and Y. Wu, *J. Am. Ceram. Soc.* **103**, 750 (2020).
- [6] R.-Z. Zhang, F. Gucci, H. Zhu, K. Chen, and M. J. Reece, *Inorg. Chem.* **57**, 13027 (2018).
- [7] J. Zhou, J. Zhang, F. Zhang, B. Niu, L. Lei, and W. Wang, *Ceram. Int.* **44**, 22014 (2018).
- [8] T. Wen, H. Liu, B. Ye, D. Liu, and Y. Chu, *Sci. China Mater.* **63**, 300 (2020).
- [9] T. Jin, X. H. Sang, R. R. Unocic, R. T. Kinch, X. F. Liu, J. Hu, H. L. Liu, and S. Dai, *Adv. Mater.* **30**, 1707512 (2018).
- [10] R. Djenadic, A. Sarkar, O. Clemens, C. Loho, M. Botros, V. S. K. Chakravadhanula, C. Kübel, S. S. Bhattacharya, A. S. Gandhi, and H. Hahn, *Mater. Res. Lett.* **5**, 102 (2017).
- [11] A. J. Wright and J. Luo, *J. Mater. Sci.* **55**, 9812 (2020).
- [12] C. Kinsler-Fedon, Q. Zheng, Q. Huang, E. S. Choi, J. Yan, H. Zhou, D. Mandrus, and V. Keppens, *Phys. Rev. Mater.* **4**, 104411 (2020).
- [13] K. Zhang, W. Li, J. Zeng, T. Deng, B. Luo, H. Zhang, and X. Huang, *J. Alloys Compd.* **817**, 153328 (2020).
- [14] D. A. Vinnik, E. A. Trofimov, V. E. Zhivulin, O. V. Zaitseva, S. A. Gudkova, A. Y. Starikov, D. A. Zherebtsov, A. A. Kirsanova, M. Hasner, and R. Niewa, *Ceram. Int.* **45**, 12942 (2019).
- [15] D. A. Vinnik, E. A. Trofimov, V. E. Zhivulin, O. V. Zaitseva, D. A. Zherebtsov, A. Y. Starikov, D. P. Sherstyuk, S. A. Gudkova, and S. V. Taskaev, *Ceram. Int.* **46**, 9656 (2020).
- [16] J. Dąbrowa, M. Stygar, A. Mikuła, A. Knapik, K. Mroczka, W. Tejchman, M. Danielewski, and M. Martin, *Mater. Lett.* **216**, 32 (2018).
- [17] B. Musicó, Q. Wright, T. Z. Ward, A. Grutter, E. Arenholz, D. Gilbert, D. Mandrus, and V. Keppens, *Phys. Rev. Mater.* **3**, 104416 (2019).
- [18] C. M. Rost, E. Sachet, T. Borman, A. Moballegh, E. C. Dickney, D. Hou, J. L. Jones, S. Curtarolo, and J.-P. Maria, *Nat. Commun.* **6**, 8485 (2015).
- [19] B. L. Musicó, D. Gilbert, T. Z. Ward, K. Page, E. George, J. Q. Yan, D. Mandrus, and V. Keppens, *APL Mater.* **8**, 040912 (2020).

- [20] Q. Wang, A. Sarkar, D. Wang, L. Velasco, R. Azmi, S. S. Bhattacharya, T. Bergfeldt, A. Düvel, P. Heitjans, T. Brezesinski *et al.*, *Energy Environ. Sci.* **12**, 2433 (2019).
- [21] C. N. R. Rao and B. Raveau, *Colossal Magnetoresistance, Charge Ordering and Related Properties of Manganese Oxides* (World Scientific, Singapore, 1998).
- [22] B. Raveau and M. Seikh, *Cobalt Oxides: From Crystal Chemistry to Physics* (Wiley, New York, 2012).
- [23] M. Lorenz, M. S. Ramachandra Rao, T. Venkatesan, E. Fortunato, P. Barquinha, R. Branquinho, D. Salgueiro, R. Martins, E. Carlos, A. Liu *et al.*, *J. Phys. D: Appl. Phys.* **49**, 433001 (2016).
- [24] A. R. Mazza, E. Skoropata, Y. Sharma, J. Lapano, T. W. Heitmann, B. L. Musico, V. Keppens, Z. Gai, J. W. Freeland, T. R. Charlton *et al.*, *Adv. Sci.* **9**, 2200391 (2022).
- [25] N. Dragoe and D. Bérardan, *Science* **366**, 573 (2019).
- [26] E. P. George, D. Raabe, and R. O. Ritchie, *Nat. Rev. Mater.* **4**, 515 (2019).
- [27] G. K. P. Dathar, J. Balachandran, P. R. C. Kent, A. J. Rondinone, and P. Ganesh, *J. Mater. Chem. A* **5**, 1153 (2017).
- [28] K. P. Tseng, Q. Yang, S. J. McCormack, and W. M. Kriven, *J. Am. Ceram. Soc.* **103**, 569 (2020).
- [29] P. B. Meisenheimer, L. D. Williams, S. H. Sung, J. Gim, P. Shafer, G. N. Kotsonis, J.-P. Maria, M. Trassin, R. Hovden, E. Kioupakis, and J. T. Heron, *Phys. Rev. Mater.* **3**, 104420 (2019).
- [30] T. Goko, C. J. Arguello, A. Hamann, T. Wolf, M. Lee, D. Reznik, A. Maisuradze, R. Khasanov, E. Morenzoni, and Y. J. Uemura, *npj Quantum Mater.* **2**, 44 (2017).
- [31] S. Jiang, T. Hu, J. Gild, N. Zhou, J. Nie, M. Qin, T. Harrington, K. Vecchio, and J. Luo, *Scr. Mater.* **142**, 116 (2018).
- [32] D. Bérardan, S. Franger, A. K. Meena, and N. Dragoe, *J. Mater. Chem. A* **4**, 9536 (2016).
- [33] J. Gild, M. Samiee, J. L. Braun, T. Harrington, H. Vega, P. E. Hopkins, K. Vecchio, and J. Luo, *J. Eur. Ceram. Soc.* **38**, 3578 (2018).
- [34] A. Sarkar, L. Velasco, D. I. Wang, Q. Wang, G. Talasila, L. de Biasi, C. Kübel, T. Brezesinski, S. S. Bhattacharya, H. Hahn, and B. Breitung, *Nat. Commun.* **9**, 3400 (2018).
- [35] R. Witte, A. Sarkar, R. Kruk, B. Eggert, R. A. Brand, H. Wende, and H. Hahn, *Phys. Rev. Mater.* **3**, 034406 (2019).
- [36] J. L. Braun, C. M. Rost, M. Lim, A. Giri, D. H. Olson, G. N. Kotsonis, G. Stan, D. W. Brenner, J.-P. Maria, and P. E. Hopkins, *Adv. Mater.* **30**, 1805004 (2018).
- [37] J. Zhang, J. Yan, S. Calder, Q. Zheng, M. A. McGuire, D. L. Abernathy, Y. Ren, S. H. Lapidus, K. Page, H. Zheng *et al.*, *Chem. Mater.* **31**, 3705 (2019).
- [38] M. P. Jimenez-Segura, T. Takayama, D. Bérardan, A. Hoser, M. Reehuis, H. Takagi, and N. Dragoe, *Appl. Phys. Lett.* **114**, 122401 (2019).
- [39] P. B. Meisenheimer, T. J. Kratochvil, and J. T. Heron, *Sci. Rep.* **7**, 13344 (2017).
- [40] A. Sarkar, R. Djenadic, D. Wang, C. Hein, R. Kautenburger, O. Clemens, and H. Hahn, *J. Eur. Ceram. Soc.* **38**, 2318 (2018).
- [41] F. Okejiri, Z. Zhang, J. Liu, M. Liu, S. Yang, and S. Dai, *ChemSusChem* **13**, 111 (2020).
- [42] Y. Pu, Q. Zhang, R. Li, M. Chen, X. Du, and S. Zhou, *Appl. Phys. Lett.* **115**, 223901 (2019).
- [43] R. Das, S. Bhattacharya, A. Haque, D. Ghosh, O. I. Lebedev, A. Gayen, and M. M. Seikh, *J. Magn. Magn. Mater.* **538**, 168267 (2021).
- [44] R. Witte, A. Sarkar, L. Velasco, R. Kruk, R. A. Brand, B. Eggert, K. Ollefs, E. Weschke, H. Wende, and H. Hahn, *J. Appl. Phys.* **127**, 185109 (2020).
- [45] A. Sarkar, R. Kruk, and H. Hahn, *Dalton Trans.* **50**, 1973 (2021).
- [46] L. M. Rodríguez-Martínez and J. P. Attfield, *Chem. Mater.* **11**, 1504 (1999).
- [47] A. Maignan, C. Martin, G. Van Tendeloo, M. Hervieu, and B. Raveau, *Phys. Rev. B* **60**, 15214 (1999).
- [48] C. N. R. Rao, A. K. Kundu, M. M. Seikh, and L. Sudheendra, *Dalton Trans.* **19**, 3003 (2004).
- [49] P. Chen, W. He, G. Xiao, J. Wen, T. Yang, X. Wu, and T. Wang, *J. Appl. Phys.* **127**, 055110 (2020).
- [50] S. Banik and I. Das, *J. Alloys Compd.* **742**, 248 (2018).
- [51] Y. Li, H. Zhang, Q. Chen, D. Li, Z. Li, and Y. Zhang, *Ceram. Int.* **44**, 5378 (2018).
- [52] S. Banik, K. Das, and I. Das, *RSC Adv.* **7**, 16575 (2017).
- [53] H. Y. Hwang, S. W. Cheong, P. G. Radaelli, M. Marezio, and B. Batlogg, *Phys. Rev. Lett.* **75**, 914 (1995).
- [54] V. M. Goldschmidt, *Naturwissenschaften* **14**, 477 (1926).
- [55] O. Clemens, M. Gröting, R. Witte, J. M. Perez-Mato, C. Loho, F. J. Berry, R. Kruk, K. S. Knight, A. J. Wright, H. Hahn, and P. R. Slater, *Inorg. Chem.* **53**, 5911 (2014).
- [56] O. Clemens, M. Kuhn, and R. Haberkorn, *J. Solid State Chem.* **184**, 2870 (2011).
- [57] R. D. Shannon, *Acta Cryst. A* **32**, 751 (1976).
- [58] A. Sarkar, R. Djenadic, N. J. Usharani, K. P. Sanghvi, V. S. Chakravadhanula, A. S. Gandhi, H. Hahn, and S. S. Bhattacharya, *J. Eur. Ceram. Soc.* **37**, 747 (2017).
- [59] A. Urushibara, Y. Moritomo, T. Arima, A. Asamitsu, G. Kido, and Y. Tokura, *Phys. Rev. B* **51**, 14103 (1995).
- [60] A. Hossain, D. Ghosh, U. Dutta, P. S. Walke, N. E. Mordvinova, O. I. Lebedev, B. Sinha, K. Pal, A. Gayen, A. K. Kundu, and M. M. Seikh, *J. Magn. Magn. Mater.* **444**, 68 (2017).
- [61] J. Rodriguez-Carvajal, An Introduction to the Program Fullprof, 2000 (Laboratoire Leon Brillouin, CEA-CNRS, Saclay, France, 2001), p. 1257.
- [62] See Supplemental Material at <http://link.aps.org/supplemental/10.1103/PhysRevMaterials.7.024411> for refinement and structural parameters, cell parameters, bond lengths and their variation with  $\langle r_A \rangle$ , imaging, EDX spectra, elemental mapping, XPS analysis, temperature derivative of magnetization ( $dM/dT$ ), and isothermal magnetization.
- [63] A. Venkatesan, N. R. K. Chandar, A. Kandasamy, M. K. Chinnu, K. N. Marimuthu, R. M. Kumar, and R. Jayavel, *RSC Adv.* **5**, 21778 (2015).
- [64] N. J. Shivaramu, E. Coetsee, W. D. Roos, K. R. Nagabhushana, and H. C. Swart, *J. Phys. D: Appl. Phys.* **53**, 475305 (2020).
- [65] P. Abbasi, M. R. Barone, M. de la Paz Cruz-Jáuregui, D. Valdespino-Padilla, H. Paik, T. Kim, L. Kornblum, D. G. Schlom, T. A. Pascal, and D. P. Fenning, *Nano Lett.* **22**, 4276 (2022).
- [66] B. Poojitha, R. Shukla, M. Vasundhara, U. M. Rasi, R. B. Gangineni, S. C. Sahoo, R. J. Choudhary, Y. Bitla, and A. K. Patra, *J. Magn. Magn. Mater.* **530**, 167851 (2021).

- [67] J. J. Dolo, H. C. Swart, J. J. Terblans, E. Coetsee, O. M. Ntwaeaborwa, and B. F. Dejene, *Phys. B (Amsterdam, Neth.)* **407**, 1586 (2012).
- [68] N. Khan, A. Midya, K. Mydeen, P. Mandal, A. Loidl, and D. Prabhakaran, *Phys. Rev. B* **82**, 064422 (2010).
- [69] N. Menyuk, P. M. Raccach, and K. Dwight, *Phys. Rev.* **166**, 510 (1968).
- [70] K. Ghosh, C. J. Lobb, R. L. Greene, S. G. Karabashev, D. A. Shulyatev, A. A. Arsenov, and Y. Mukovskii, *Phys. Rev. Lett.* **81**, 4740 (1998).
- [71] Y. Kalyana Lakshmi, G. Venkataiah, and P. V. Reddy, *J. Appl. Phys.* **106**, 023707 (2009).
- [72] L. Liu, Y. Liu, J. Miao, Z. Lü, X. Wang, Y. Sui, Z. Liu, Y. Li, Q. Huang, D. Shang, and W. Su, *J. Alloy. Compd.* **427**, 11 (2007).
- [73] A. Elhamza, F. I. H. Rhouma, J. Dhahri, and E. K. Hlil, *Appl. Phys. A* **123**, 358 (2017).
- [74] S. Saha, A. Dutta, S. Gupta, S. Bandyopadhyay, and I. Das, *Phys. Rev. B* **105**, 214407 (2022).
- [75] L. M. Rodriguez-Martinez and J. P. Attfield, *Phys. Rev. B* **54**, R15622 (1996).
- [76] F. Sher, A. Venimadhav, M. G. Blamire, K. Kamenev, and J. P. Attfield, *Chem. Mater.* **17**, 176 (2005).
- [77] Y. Tokura, *Rep. Prog. Phys.* **69**, 797 (2006).
- [78] A. Berenov, F. Le Goupil, and N. Alford, *Sci. Rep.* **6**, 28055 (2016).
- [79] Y. Moritomo, H. Kuwahara, Y. Tomioka, and Y. Tokura, *Phys. Rev. B* **55**, 7549 (1997).
- [80] R. Mathieu, M. Uchida, Y. Kaneko, J. P. He, X. Z. Yu, R. Kumai, T. Arima, Y. Tomioka, A. Asamitsu, Y. Matsui, and Y. Tokura, *Phys. Rev. B* **74**, 020404(R) (2006).
- [81] B. Raveau, A. Maignan, and V. Caignaert, *J. Solid State Chem.* **117**, 424 (1995).
- [82] R. Mahesh, R. Mahendiran, A. K. Raychaudhuri, and C. N. R. Rao, *J. Solid State Chem.* **120**, 204 (1995).
- [83] S. Jin, H. M. O'Bryan, T. M. Tiefel, M. McCormack, and W. W. Rhodes, *Appl. Phys. Lett.* **66**, 382 (1995).
- [84] M. M. Seikh, L. Sudheendra, and C. N. R. Rao, *J. Solid State Chem.* **177**, 3633 (2004).
- [85] G. M. Zhao, K. Conder, H. Keller, and K. A. Müller, *Nature (London)* **381**, 676 (1996).
- [86] H. Kuwahara, Y. Tomioka, Y. Moritomo, A. Asamitsu, M. Kasai, R. Kumai, and Y. Tokura, *Science* **272**, 80 (1996).
- [87] A. Asamitsu, Y. Moritomo, Y. Tomioka, T. Arima, and Y. Tokura, *Nature (London)* **373**, 407 (1995).
- [88] R. Mahendiran, S. K. Tiwary, A. K. Raychaudhuri, T. V. Ramakrishnan, R. Mahesh, N. Rangavittal, and C. N. R. Rao, *Phys. Rev. B* **53**, 3348 (1996).
- [89] K. F. Wang, Y. Wang, L. F. Wang, S. Dong, D. Li, Z. D. Zhang, H. Yu, Q. C. Li, and J. M. Liu, *Phys. Rev. B* **73**, 134411 (2006).
- [90] M. Otero-Leal, F. Rivadulla, and J. Rivas, *Phys. Rev. B* **76**, 174413 (2007).
- [91] M. B. Salamon, P. Lin, and S. H. Chun, *Phys. Rev. Lett.* **88**, 197203 (2002).
- [92] W. Jiang, X. Zhou, G. Williams, Y. Mukovskii, and K. Glazyrin, *Phys. Rev. Lett.* **99**, 177203 (2007).
- [93] R. B. Griffiths, *Phys. Rev. Lett.* **23**, 17 (1969).
- [94] B. M. McCoy, *Phys. Rev. Lett.* **23**, 383 (1969).
- [95] M. B. Salamon, and Chun, *Phys. Rev. B* **68**, 014411 (2003).
- [96] A. K. Pramanik and A. Banerjee, *Phys. Rev. B* **81**, 024431 (2010).
- [97] P. Tong, B. Kim, D. Kwon, T. Qian, S. I. Lee, S. W. Cheong, and B. G. Kim, *Phys. Rev. B* **77**, 184432 (2008).
- [98] K. F. Wang, F. Yuan, S. Dong, D. Li, Z. D. Zhang, Z. F. Ren, and J. M. Liu, *Appl. Phys. Lett.* **89**, 222505 (2006).
- [99] K. F. Wang, W. Z. Luo, S. Dong, D. Li, Z. D. Zhang, Z. F. Ren, and J. M. Liu, *Thin Solid Films* **518**, e38 (2010).
- [100] M. K. Srivastava, R. Prasad, P. K. Siwach, M. P. Singh, and H. K. Singh, *J. Appl. Phys.* **107**, 09D726 (2010).
- [101] D. Zhu, X. Tan, P. Cao, F. Jia, X. Ma, and Y. Lu, *J. Appl. Phys.* **105**, 063914 (2009).
- [102] Y. Tomioka and Y. Tokura, *Phys. Rev. B* **70**, 014432 (2004).
- [103] C. Autret, C. Martin, M. Hervieu, A. Maignan, B. Raveau, G. André, F. Bourée, and Z. Jirak, *Chem. Mater.* **15**, 1886 (2003).